Elsevier Editorial System(tm) for
Construction & Building Materials
Manuscript Draft

Manuscript Number: CONBUILDMAT-D-18-04365R1

Title: End-repair of timber beams with laterally-loaded glued-in rods: experimental trials and failure prediction through modelling

Article Type: Research Paper

Keywords: Timber elements reinforcing; Perpendicular-to-grain strength; Continuum Damage Mechanics; FE modelling; Photogrammetry

Corresponding Author: Dr. Benedetto Pizzo, Ph.D.

Corresponding Author's Institution: CNR-IVALSA

First Author: Nicola Orlando, Ph.D.

Order of Authors: Nicola Orlando, Ph.D.; Yuri Taddia, Dr.; Elena Benvenuti, Prof.; Benedetto Pizzo, Ph.D.; Claudio Alessandri, Prof.

Abstract: Experimental trials were performed on spruce beams with one end cut and re-connected with glued-in rods to simulate repair interventions. Beams were tested in bending thus to laterally load rods, and documented by photogrammetry. Numerical analysis, adopting orthotropic constitutive laws in the context of the Continuum Damage Mechanics, was also performed. Results showed that short screws did not improve the load capacity but affected the failure mechanism. Numerical simulation correctly predicted the load-displacement curves, the damage maps, and the deflection behaviour. It was established that failure is related to a combination of perpendicular-to-grain tension, longitudinal shear and rolling shear.

***Highlights**

Paper title: End-repair of timber beams with laterally-loaded glued-in rods: experimental trials and failure prediction through modelling

Authors: Nicola Orlando, Yuri Taddia, Elena Benvenuti, Benedetto Pizzo, Claudio Alessandri

Highlights:

- Spruce beams repaired with glued-in rods were tested in bending (laterally loaded rods)
- Photogrammetric measures and numerical results obtained with an orthotropic Continuum Damage Model
- Short screws do not improve load capacity but affect the failure mechanism
- Numerical simulations predict load-displacement curves, damage maps and deflection
- Failure due to perpendicular-to-grain tension, longitudinal shear and rolling shear

End-repair of timber beams with laterally-loaded glued-in rods: experimental trials and failure prediction through modelling

Nicola Orlando [a], Yuri Taddia [a], Elena Benvenuti [a], Benedetto Pizzo [b,*], Claudio Alessandri [a]

[a] Department of Engineering, University of Ferrara, via Saragat 1, I-44122, Ferrara, Italy

[b] CNR-IVALSA, Istituto per la Valorizzazione del Legno e delle Specie Arboree, via Madonna del Piano 10, I-50019, Sesto Fiorentino (FI), Italy

* Corresponding author
Benedetto Pizzo
e-mail: pizzo@ivalsa.cnr.it
postal address: CNR-IVALSA, via Madonna del Piano 10, I-50019, Sesto Fiorentino (FI), Italy
Fax: +39 055 522 5507

Abstract

Experimental trials were performed on spruce beams with one end cut and re-connected with glued-in rods to simulate repair interventions. Beams were tested in bending thus to laterally load rods, and documented by photogrammetry. Numerical analysis, adopting orthotropic constitutive laws in the context of the Continuum Damage Mechanics, was also performed. Results showed that short screws did not improve the load capacity but affected the failure mechanism. Numerical simulation correctly predicted the load-displacement curves, the damage maps, and the deflection behaviour. It was established that failure is related to a combination of perpendicular-to-grain tension, longitudinal shear and rolling shear.

Keywords: Timber elements reinforcing, Perpendicular-to-grain strength, Continuum Damage Mechanics, FE modelling, Photogrammetry

1 Introduction

During their service life timber structures may need reinforcing interventions due to several reasons, including repair when decay has occurred [1]. In fact, specific parts of timber elements (such as the ends, usually in contact with masonry) are under high risk of biotic attack because excessive levels of humidity may possibly develop in walls (e.g., after malfunctioning of rain-collecting systems, associated to lack of adequate maintenance) [2].

In the events mentioned above, which can be related to both old and new buildings, several reinforcing techniques can be proposed, making use of either steel or FRP elements [3–5]. Among them, the use of glued-in rods (GIR) placed into predrilled holes or slots and bonded with structural adhesives, represents a good solution for possible interventions; in fact, the joints prepared with GIR are considered to possess high strength and stiffness along the rod axis, low cost for the preparation, improved fire resistance and good aesthetic appearance, due to both hidden connecting elements and low loss of original timber [6,7]. This latter characteristic is mostly important in the conservation of timber elements in heritage monuments, as in this case the safeguarding authorities prescribe that the original parts are maintained integer as much as possible, even when structural upgrading is needed. Thus, the use of interventions making use of GIR is a realistic and successful alternative to the replacement of whole elements that are only partially decayed, provided that these interventions are consistent with heritage conservation principles [8]. This is the case of the Church of the Nativity in Bethlehem where this technique was recently used for the restoration of some of the wooden roof trusses on the basis of indications previously provided [9].

However, the majority of research carried out on GIR has been oriented towards rods glued into wood elements under purely axial loading. Already in these conditions bars are subjected to both uneven stress distribution along their length (peaks at both rod ends) and stresses perpendicular to the axis [10–12]. Furthermore, in lateral loading conditions, such as those characterising the interventions on beam-ends or on spliced beams (both are moment resisting connections), a multiaxial system of forces is involved, which makes the stress distribution much more complex to manage. In fact, mechanical response of wood under multi-axial stress states has been considered only rarely [13], and little is known about failure behaviour of timber under combined stresses [14].

It is worthwhile observing that even in the case of uniaxial forces nominally acting on the bars the design approach is not fully established among researchers, and no unique design codes exist at European level for this typology [15]. Actually, Eurocode 5 [16] does not take into account this specific type of connection. Thus, it can be easily understood how no reliable rules to predict the mechanical performance are yet available for the case of multiaxial stress distribution. Accordingly, the usual approach encountered in the scientific literature to characterise the load bearing capacity of such connections is based on developmental-type investigations sometimes associated to Finite Element (FE) modelling.

Experimental trials were carried out on both new and old timber beams where one of the two ends were cut and re-connected using GIR inserted in slots, so as to simulate a repair intervention on biologically decayed ends [17]. The prepared beams were tested in bending (thus, rods were laterally loaded), and results evidenced that specimens invariably failed at the repaired side and the collapse mechanism was wood splitting close to rods, which was unexpected according to the adopted design approach (based on ENV 1995-2:1997, as in some European countries). A combined effect of shear and orthogonal-to-grain tensile stresses was suggested as possible causes of collapse [17]. Splitting induced by non-axial loading was also observed in other cases of laterally loaded bars. For instance, recent tests [18] were carried out on Sitka spruce spliced beams, connected with glued-in basalt fibre reinforced polymer (BFRP) rods and subjected to pull-bending tests (combination of axial and bending forces). Results displayed that several specimens failed prematurely due to the development of splitting, and, in these cases, a lower failure strength was observed with an average drop of almost 8% [18]. Splitting of GIR reinforced wood is usually attributed to: a) short edge distances; b) rod misalignment; c) excessive loading perpendicular to the grain. This failure mode can be prevented by transversely reinforcing the connection in the proximity of bars, e.g. by means of screws [6]. This solution was already adopted in tests carried out on glued-laminated spliced beams of Norway spruce loaded in bending [19]. Moreover, new spruce beams with ends cut and repaired using steel bars and transversal screws passing from the intrados to the extrados evidenced a 30% load bearing capacity increase compared to the series without the screws [20].

The mechanical behaviour of such prostheses is made even more complex by the fact that in GIR-based connections the joint strength depends on parameters affected by both the mechanical and the geometrical

84 factors of three different materials: wood, adhesive, and reinforcing/connecting element. Thus, FE modelling
85 is often taken into consideration to interpret the results obtained in experimental tests.
86 Actually, a reliable constitutive FE model for timber has to be anisotropic and to account for both the
87 difference in strength between tension and compression and the simultaneous presence of ductile and brittle
88 failure modes. State-of-the-art-literature on FE constitutive models mostly provides anisotropic plasticity
89 models based on Tsai and Wu [21] and Hill [22] failure criteria. For instance, Bouchaïr and Vergne [23], and
90 Clouston and Lam [24] developed single-surface plasticity models by combining the classical flow theory of
91 plasticity with the elliptical Tsai and Wu failure surface for anisotropic materials [21,25]. Other examples of
92 single-surface plasticity models are based on the failure surfaces proposed by Hoffman [26], e.g. [27].
93 Although single-surface plasticity models are able to predict the failure loads of the material, they fail to
94 reproduce different failure modes, and do not satisfactorily describe the structural behaviour. Therefore, a
95 multi-surface plasticity model has been developed [28,29]. However, the parameters employed for the
96 mathematical description of the multi-surfaces may lack of direct physical meaning, while the computational
97 transition from one surface to another one is prone to numerical instabilities. An alternative approach to
98 plasticity models consists in adopting orthotropic constitutive laws in the context of Continuum Damage
99 Mechanics (CDM). In CDM models, the progressive deterioration of the mechanical strength (due for
100 instance to the development of micro-cracks) is modelled through the introduction into the stiffness matrix of
101 damage variables representative of the state of degradation of the material, ranging from 0 for sound material
102 to 1 for completely broken material. According to CDM, when a material is unloaded after the onset of
103 damage, the stress goes to zero following a damaged elastic modulus different from the initial elastic
104 modulus of the sound material. Thus, CDM is suitable to model materials whose constitutive law exhibits a
105 brittle softening post-peak branch and failure mainly occurs by strain localization. Recently, Sandhaas et al.
106 [30] have developed a simplified effective 3D material model suitable for modelling localized ruptures
107 observed in timber structures. For a complete 3D description of wood as an orthotropic material, CDM
108 model is based on eight types of brittle and ductile failure modes governed by six damage variables [31],
109 while ductile plastic-like behaviour under compression is simulated by means of an elastic-damaging law
110 displaying a horizontal stress threshold beyond a critical strain. This approach overcomes the emergence of
111 mesh-dependency induced by the presence of softening constitutive laws through the adoption of the crack-

band model [32]. Alternatively, mesh dependency can be tackled by referring to non-local elastic-damaging models, that introduce a regularization length by replacing a local field, such as an internal variable, with its volume average or gradient expansion, e.g. [33,34]. However, besides being their implementation burdensome, non-local models lead to damaged zones excessively spread over a large area as the adopted regularization length is too large compared with the material characteristic length. Thus, the adoption of the aforementioned crack-band model is an acceptable compromise between simplicity of implementation and accuracy. Furthermore, in the Sandhaas and van de Kuilen model [31], a fictitious-viscosity-based stabilization term had to be used to tackle the appearance of fast snap-back and snap-through points encountered during the loading process. Although permanent plastic deformations are not captured, it has been successfully applied to the modelling of timber specimens subjected to monotonic tension, compression and dowel embedment [30]. Advanced elastic-plastic orthotropic constitutive laws coupled with isotropic damage have been recently applied to timber elements [35,36]. However, they fail to capture the anisotropic damage pattern developing in (repaired) timber beams.

Focus of present work is to analyse in more detail the mechanical behaviour of timber beams repaired by means of solid wood prosthesis connected with steel GIR and to evaluate possible improvements of such a behaviour by using screws, as suggested in [20]. In our case, differently than what was done before, the use of short screws locally reinforcing the elements in the perpendicular-to-grain direction and placed close to the rod insertion areas is considered in the attempt of limiting the use of long screws (mostly impacting for large-sized beams). Four-point-bending tests were carried out in the Laboratory on spruce repaired beams up to the final collapse, and documented by photogrammetric surveys. Such experimental tests offered the opportunity of validating the mentioned 3D-CDM model to predict the load carrying capacity in bending of repaired beams. In fact, to the authors' knowledge, FE simulations of timber beams end-repaired with wood prosthesis, GIR steel bars and reinforcing screws have yet to be done. It is also worth evidencing that adopting in present work a more robust arc-length algorithm than those generally available in commercial codes made it possible to steadily follow the structural behaviour without the need of introducing spurious viscosity terms of ambiguous physical meaning.

2 Materials and Methods

2.1 Samples and test apparatus

A total of 15 glulam, simply supported beams (cross section 120 x 160 mm^2; span length 1800 mm), graded as GL28h and made of Norway spruce (*Picea abies* Karst.) were analysed in 4-points bending tests (**Fig 1a**, **1b** and **1c**). The various specimens were cut close to one end and then the two parts were re-sewed using 4 steel bars (S275, nominal diameter 10 mm, length 400 mm) glued into specifically prepared slots by means of epoxy adhesive (Mapewood Paste 140). In this way, the variability related to wood characteristics (density, slope of grain, moisture content, ageing effects etc.) on joint performances was kept to a minimum. The transversal geometry of specimens is shown in **Fig 2**. Rods were placed parallel to wood grain, and slots had a square section, as usual in interventions carried out onsite [37,38]. Bars were centred along each slot using stoppers, thus ensuring an equal anchorage length between the two parts of the beam. Additionally, to arrange a proper centring, O-rings were used at rod ends.

Beams were divided into three groups (each consisting of five specimens) (**Fig 1**):

i) (configuration 45/refer) cut inclined 45° with respect to the geometrical axis. Considering that in normal practice no reinforcing screws are used, this configuration is assumed as the reference one for beams with 45° inclined cut (**Fig 1a**) both in experimental and numerical tests;

ii) (configuration 45/45) cut inclined 45° and use of 16 reinforcing screws (ø 6 mm, length 160 mm), 8 on each part of the beam, also inclined 45° compared to the wood grain/geometrical axis. The screws insertion pattern is shown in **Fig 1b** and **Fig 2**. The length of reinforcing screws (160 mm) was selected based on previous tests [17], which showed that in the reference configuration the majority of specimens failed under the upper bar of the main part (the longer one) of the beam and above the lower bar of prosthesis (the shorter one) [17]. Therefore, the screws are stopped before the opposite rod;

iii) (configuration 90/90) cut inclined 90° (vertical) and use of 16 reinforcing screws (ø 6 mm, length 120 mm), 8 on each part of the beam, inserted perpendicular to wood grain. The screws insertion pattern is shown in **Fig 1c**. The length of the screws was chosen with the same rational as described in point (ii). It is worth noting that beams with 90° inclined cut, but without screws, were not tested because previous

experiences proved the irrelevant influence of the cut orientation on the mechanical behaviour of the whole beam [20].

Beams were left to cure for a minimum of 15 days in standard conditions (20°C and 65% r.h.). The 4-points bending tests were configured so as to make appreciable the shear stress close to the repaired end-parts (**Fig 1**), as usually occurs in real cases (where prostheses are close to walls). Tests were carried out on a Z600 universal testing machine (produced by Zwick/Roell) with 600kN load capacity (load cell accuracy ±1%).

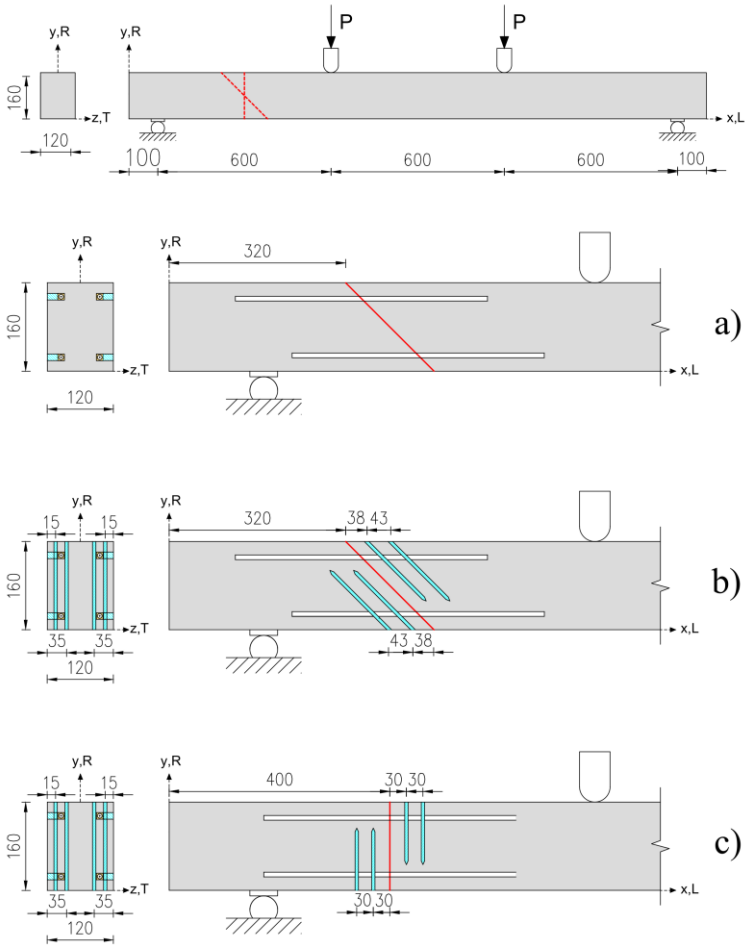

Fig 1 - Specimen configurations and test arrangements: (a) the reference one (cut inclined 45°, no reinforcing screws); (b) same as (a) but with the use of reinforcing screws inclined 45° compared to wood grain; (c) configurations with vertical cut and perpendicular-to-grain reinforcing screws.

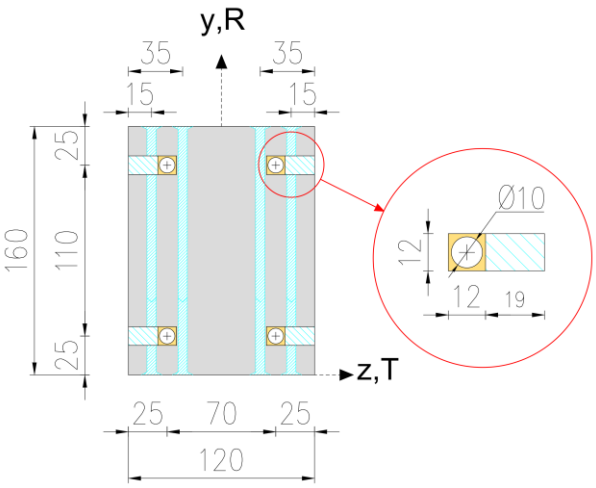

179

180 **Fig 2** - Scheme of the transversal section of all repaired beams. The position of screws is also visible in the

181 cross-section.

182

183 Firstly, beams were subjected to 2 preliminary load steps from 0 to 12 kN; then, load was gradually

184 increased at a load-bar rate of 7.5 mm/min up to collapse. The load-displacement curve was acquired using

185 the built-in LVDT transducer provided with the dynamometer; thus, the displacement of the upper loading

186 anvils was actually measured. This measurement was also compared with the photogrammetric acquisitions

187 described in Section 2.2.

188

189 *2.2 Arrangement for photogrammetric survey*

190 Many different techniques have been tested and compared over the years [39] to detect deflections, such as

191 terrestrial laser scanners [40,41], total stations [42] and digital photogrammetry [43–45].

192 The close range photogrammetry is a no contact technique that exploits the metric data retrievable from a set

193 of images characterized by an accuracy related to the geometric resolution and depending on the real pixel

194 size, the so-called Ground Sample Distance (GSD). Assuming that the pixel size (ps) on the sensor plane

195 array is known, the GSD is given by the following expression:

196 $$GSD = ps \cdot \frac{d}{f} \quad . \tag{1.1}$$

197 where d is the distance from the perspective center to the beam's surface and f is the principal distance that is

198 very close to the focal length after the calibration process. By collecting data at a distance of about 1.5

meters between the camera and the surface of the beam, it is possible to reach a GSD between 0.15 and 0.35 mm.

It is also worth noting that photogrammetry allows following the deflection process up to the final collapse of the beam without issues related to the range of measure due to the limited length of rod's transducers. Moreover, photogrammetry allows making a global and punctual check at the same time during the whole deflection process.

For all the above reasons, its accuracy and very high resolution at a few meter distance [46], the close range photogrammetry was therefore used to perform all the deflection measurements. It is worth noting that in the experimental tests presented in this paper it was necessary to take pictures of the beam at a high rate to assess the cracks occurrence and evolution during the whole bending test.

In order to do this, 12 targets (**Fig 3**) connected to the bending machine's frame, were located on the same plane of the photographed face of the beam and surveyed with a precise Leica TS06 total station. The targets were assumed to be stable during the whole duration of the test.

Fig 3 - Location of targets and sample beam prepared for photogrammetric detection.

To ensure that no significant temporal offset would affect the relation between deflection and actual load, a well visible chronometer was placed near the left bottom targets and manually synchronized with the data recorded by the load cell.

The photogrammetric measurement system was previously developed by simulating displacements in laboratory and by detecting them through a MATLAB script. During these preliminary tests, the displacements were imposed and known with an accuracy of few micrometers (**Fig 4**).

Fig 4 - On the left: device for micrometric displacement imposition. On the right: image acquisition during preliminary tests for automatic displacement detection.

The discrepancies between the imposed displacement and the corresponding ones turned out to be less than the GSD for the whole set of measurements.

Two different cameras were therefore used to document each bending test: a Canon EOS 7D (18 Megapixel) equipped with very low distortion lens at a fixed focal length of 35 mm for acquiring detail on the end-repaired beam and a Canon EOS M with a focal length of 18 mm to capture the whole tested beam and reconstruct a displacement profile. Images acquired with the first one were directly processed through the MATLAB script, whereas the others were previously corrected for lens distortion and perspective by using total station's surveyed targets. The reason is that both distortion and perspective deformation were proved by laboratory tests to be negligible in detecting displacements in the frontal configuration with the EOS 7D camera, since the specific lens used has a very low distortion (**Fig 5**) and the effect of perspective is minimum. The calibration of both cameras was performed with PhotoModeler and is reported in Table 1, where K_1, K_2, K_3 are the coefficients of Brown's model [47] and P_1, P_2 are the decentering distortion parameters.

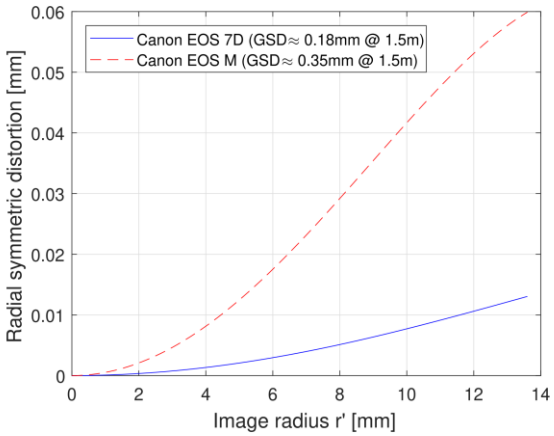

Fig 5 - Radial distortion for EOS 7D and EOS M cameras: the first one (blue) is equipped with very low distortion lens, while the second one (red) has a wide-angle lens.

A further validation of the photogrammetric acquisition system has been performed during preliminary tests carried out on selected wood beams (up to 30 kN) and using the same test arrangement: the error did not significantly exceed the GSD at any load level (data not shown).

Table 1 – Calibration parameters of the cameras.

Camera model	EOS 7D	EOS M
Principal distance [mm]	35.217	18.653
X_p (principal point x) [mm]	11.328	11.563
Y_p (principal point y) [mm]	7.672	7.399
F_w (format width) [mm]	22.681	22.740
F_h (format height) [mm]	15.113	15.164
K_1 (radial distortion 1)	8.481E-05	5.262E-04
K_2 (radial distortion 2)	-7.722E-08	-1.094E-06
K_3 (radial distortion 3)	0	0
P_1 (decentering distortion 1)	3.164E-06	-9.061E-05
P_2 (decentering distortion 2)	0	-4.208E-06
pixel size [µm]	4.375	4.387
GSD at 1.5 m distance [mm]	0.186	0.353

2.3 *Constitutive model of the FE formulation*

A high-performance 3D and parallelised Finite Element FORTRAN code has been developed by some of the authors to carry out large-scale numerical simulations of the experimental tests and to obtain numerical results to compare with the experimental ones. The present Fortran code adopts the orthotropic elastic-damaging constitutive model proposed in Sandhaas and van de Kuilen [31] with the introduction of the crack band model to alleviate the possible mesh-dependency of the numerical results induced by the presence of softening constitutive laws. Parallelisation made it also possible to save CPU time. The present section describes the constitutive modelling adopted in the proposed Finite Element formulation.

Wood is an orthotropic material and its damaging process is also orthotropic. Let the x-axis and the y-axis be aligned with the longitudinal (L) and the radial (R) directions of the wood, respectively. In the current Section, the three material directions, namely longitudinal, radial and tangential are denoted with subscripts x, y and z, respectively (**Fig 1**). Accordingly, using the Voigt notation

$$\boldsymbol{\sigma} = \left[\sigma_{xx}, \sigma_{yy}, \sigma_{zz}, \sigma_{xy}, \sigma_{yz}, \sigma_{xz}\right]^t \equiv \left[\sigma_L, \sigma_R, \sigma_T, \sigma_{LR}, \sigma_{RT}, \sigma_{LT}\right]^t \quad . \tag{1.2}$$

The orthotropic non-linear behaviour of the wood has been modelled in the CDM framework according to Sandhaas et al. [30]. In particular, the six independent damage variables, one for each stress component, have been introduced and collected in the vector:

$$\mathbf{d} = \left[d_L, d_R, d_T, d_{LR}, d_{RT}, d_{LT}\right]^t \quad , \tag{1.3}$$

We define the effective stress vector $\boldsymbol{\sigma}$ as the stress that acts on the effective resisting area, deprived of damaged parts, i.e.

$$\boldsymbol{\sigma} = \mathbf{M}\boldsymbol{\sigma} \quad , \tag{1.4}$$

where

$$\mathbf{M} = \begin{bmatrix} \frac{1}{1-d_R} & 0 & 0 & 0 & 0 & 0 \\ 0 & \frac{1}{1-d_T} & 0 & 0 & 0 & 0 \\ 0 & 0 & \frac{1}{1-d_L} & 0 & 0 & 0 \\ 0 & 0 & 0 & \frac{1}{1-d_{RT}} & 0 & 0 \\ 0 & 0 & 0 & 0 & \frac{1}{1-d_{RL}} & 0 \\ 0 & 0 & 0 & 0 & 0 & \frac{1}{1-d_{TL}} \end{bmatrix} . \tag{1.5}$$

For the subsequent derivations, it is convenient to define the damaged compliance matrix $\mathbf{C}^d$ of wood as

$$\mathbf{C}^d = \begin{bmatrix} \frac{1}{(1-d_R)E_{11}} & -\frac{\nu_{21}}{E_{22}} & -\frac{\nu_{31}}{E_{33}} & 0 & 0 & 0 \\ -\frac{\nu_{12}}{E_{11}} & \frac{1}{(1-d_T)E_{22}} & -\frac{\nu_{32}}{E_{33}} & 0 & 0 & 0 \\ -\frac{\nu_{13}}{E_{11}} & -\frac{\nu_{23}}{E_{22}} & \frac{1}{(1-d_L)E_{33}} & 0 & 0 & 0 \\ 0 & 0 & 0 & \frac{1}{(1-d_{RT})G_{12}} & 0 & 0 \\ 0 & 0 & 0 & 0 & \frac{1}{(1-d_{RL})G_{13}} & 0 \\ 0 & 0 & 0 & 0 & 0 & \frac{1}{(1-d_{TL})G_{23}} \end{bmatrix} . \quad (1.6)$$

The nominal stress $\boldsymbol{\sigma}$ can be computed as

$$\boldsymbol{\sigma} = \mathbf{D}^d \boldsymbol{\varepsilon} \quad , \quad (1.7)$$

where the damaged stiffness matrix is obtained as $\mathbf{D}^d = \left(\mathbf{C}^d\right)^{-1}$.

Eight different failure criteria are considered in the adopted model, each one corresponding to a failure surface in the principal stress space, as detailed in the following paragraphs.

- Criterion I - Failure in parallel-to-grain tension

  Brittle failure mode caused by tensile stress parallel-to-grain $\tilde{\sigma}_L > 0$ and governed by the damage variable d_L. It obeys the loading-unloading inequality

$$F_I(\sigma) = \frac{\tilde{\sigma}_L}{f_{t,L}} - 1 \le 0 \quad , \quad (1.8)$$

  where $f_{t,L}$ is the tensile strength along the longitudinal direction.

- Criterion II - Failure in parallel-to-grain compression

  Ductile failure mode caused by compressive stress parallel-to-grain $\tilde{\sigma}_L < 0$ that affects the damage variable d_L. The failure is associated with the loading-unloading inequality

$$F_{II}(\sigma) = \frac{-\tilde{\sigma}_L}{f_{c,L}} - 1 \le 0 \quad (1.9)$$

where $f_{c,L}$ is the compressive strength along the longitudinal direction.

- Criterion III/IV - Failure in perpendicular-to-grain tension

Brittle failure modes governed by tensile perpendicular-to-grain ($\tilde{\sigma}_R > 0$ and $\tilde{\sigma}_T > 0$), longitudinal shear ($\tilde{\sigma}_{LR}, \tilde{\sigma}_{LT}$) and rolling shear ($\tilde{\sigma}_{RT}$) stresses. They are characterized by the development of splitting cracks in LR-plane and LT-plane, respectively, and are related to the damage variables d_R, d_T, d_{LR}, d_{LT} and d_{RT}. The quadratic loading-unloading inequalities:

$$F_{III}(\sigma) = \frac{\tilde{\sigma}_R^{\,2}}{f_{t,\mathrm{R}}^{\,2}} + \frac{\tilde{\sigma}_{LR}^{\,2}}{f_{v,LR}^{\,2}} + \frac{\tilde{\sigma}_{RT}^{\,2}}{f_{v,RT}^{\,2}} - 1 \le 0 \qquad and \qquad F_{IV}(\sigma) = \frac{\tilde{\sigma}_T^{\,2}}{f_{t,T}^{\,2}} + \frac{\tilde{\sigma}_{LT}^{\,2}}{f_{v,LT}^{\,2}} + \frac{\tilde{\sigma}_{RT}^{\,2}}{f_{v,RT}^{\,2}} - 1 \le 0 \quad , \tag{1.10}$$

are adopted, where $f_{t,R}$ is the tensile strength along the radial direction, $f_{t,T}$ is the tensile strength along the tangential direction, $f_{v,LR}$ is the shear strength along the LR plane, $f_{v,LT}$ is the shear strength along the LT plane, and, finally, $f_{v,RT}$ is the rolling shear strength of the material.

- Criterion V/VI - Failure in perpendicular-to-grain compression

Ductile failure modes caused by the compressive stress along the radial or the tangential direction $\tilde{\sigma}_R < 0$ and $\tilde{\sigma}_T < 0$, and governed by the damage variables d_R and d_T. They are associated with the following loading-unloading inequalities:

$$F_V(\sigma) = \frac{-\tilde{\sigma}_R}{f_{\mathrm{c,R}}} - 1 \le 0 \qquad and \qquad F_{VI}(\sigma) = \frac{-\tilde{\sigma}_T}{f_{\mathrm{c,T}}} - 1 \le 0 \quad , \tag{1.11}$$

where $f_{c,R}$ and $f_{c,T}$ are the compressive strength along the radial direction and along the tangential direction, respectively.

- Criterion VII/VIII - Shear failure

Brittle failure modes induced by the longitudinal shear stress $\tilde{\sigma}_{LR}$ and $\tilde{\sigma}_{LT}$ and the rolling shear stress $\tilde{\sigma}_{RT}$, in the case that a compressive perpendicular-to-grain $\sigma_{R/T} < 0$ occurs. They are governed by the damage variables d_{LR}, d_{LT} and d_{RT}. The current case is governed by the quadratic loading-unloading inequalities:

$$F_{VII}(\sigma)=\frac{\tilde{\sigma}_{LT}{}^{2}}{f_{v,LT}{}^{2}}+\frac{\tilde{\sigma}_{RT}{}^{2}}{f_{v,RT}{}^{2}}-1\le 0 \qquad and \qquad F_{VIII}(\sigma)=\frac{\tilde{\sigma}_{LT}{}^{2}}{f_{v,LT}{}^{2}}+\frac{\tilde{\sigma}_{RT}{}^{2}}{f_{v,RT}{}^{2}}-1\le 0 \quad . \qquad (1.12)$$

In general, the loading-unloading Kuhn-Tucker conditions for the multi-surface CDM model are cast as

$$\phi_m(\boldsymbol{\sigma},k_m)=F_m-k_m\le 0 \qquad \dot{k}_m\ge 0 \qquad \phi_m\dot{k}_m=0 \qquad m=I,\ldots,VIII \quad , \qquad (1.13)$$

where k_m is the state variable related to the *m*-th failure criteria, and $\dot{k_m}$ denotes the increment of k_m evaluated with respect to a fictitious time parameter.

In order to simulate both brittle and ductile failure modes, the Sandhaas et al. model [30] considers two damaging laws. In particular, Fig 6a shows a qualitative representation of the adopted stress-strain law adopted for each case of ductile failure mode, such as failure by compression in the parallel-to-grain and perpendicular-to-grain directions. In this case, the relevant damage variable, that is activated when the loading function is greater than zero, is calculated as:

$$d_i(k_m)=1-\frac{1}{k_m} \qquad i=L,R \quad . \qquad (1.14)$$

For each brittle failure mode induced by tensile and/or shear stresses, the bilinear softening stress-strain law displayed in **Fig 6b** is used. In this case, the damage variables related to tensile failure modes are computed according to:

$$d_i(k_m)=1-\frac{1}{f_{t.i}-2g_{f,i}E_i}\left(f_{t,i}-\frac{2g_{f,i}E_i}{k_m}\right) \qquad i=L,R,\mathrm{T} \quad , \qquad (1.15)$$

while, for shear failure modes, the damage variables are defined as:

$$d_i(k_m)=1-\frac{1}{f_{\mathrm{v}.i}-2g_{f,v,i}G_i}\left(f_{v,i}-\frac{2g_{f,\mathrm{v},i}G_i}{k_m}\right) \qquad i=LR,LT,RT \quad , \qquad (1.16)$$

$g_{f,i}$ and $g_{f,v,i}$ being the specific fracture energies for the tensile and the shear failure modes, respectively.

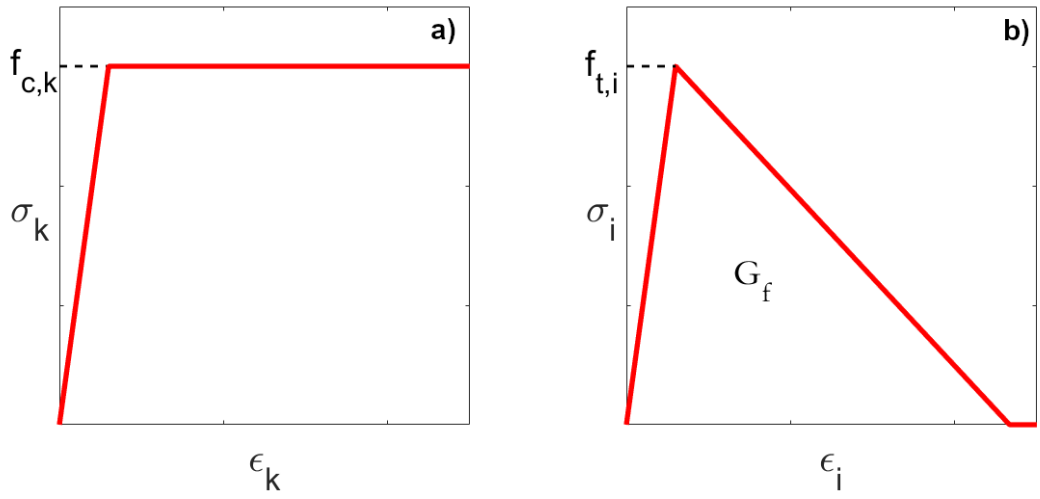

Fig 6 – Qualitative representation of the stress-strain laws adopted for: a) ductile failure modes, where k = L,R,T; b) brittle failure modes, where i = L, R, T, LR, LT, RT.

Mesh-dependency is alleviated by adopting the crack band model [32], where the specific fracture energy g_f of the single FE e is related to the fracture energy of the material G_f and to the characteristic size of the finite element h_e through

$$g_f = \frac{G_f}{h_e} \quad . \tag{1.17}$$

Fracture energies have been taken from Sandhaas and van de Kuilen [31] and Mackenzie-Helnwein et al. [28] and the other properties from Kretschmann [48] (Table 2).

Table 2 – Material parameter of Norway spruce employed for the numerical simulations.

Elastic Properties [MPa]				
E_L	E_T	E_R	$G_{LT} = G_{LR}$	G_{RT}
11000	500	800	690	50
Strengths [MPa]				
$f_{t,L}$	$f_{c,L}$	$f_{t,R} = f_{t,T}$	$f_{c,L} = f_{c,T}$	$f_{v,RT} = f_{v,RL} = f_{v,RL}$
45 - 65	25 - 35	0.5 - 2.5	3.8	4 - 6.9
Fracture Energies [N/mm]				
$G_{f,L}$	$G_{f,R} = G_{f,T}$	$G_{f,v,RL}$	$G_{f,RT}$	
2	0.3	1.2	0.6	

The 3D FORTRAN FE code was validated by modelling experimental 4-point bending tests carried out on four integer Norway spruce beams. The experimental and numerical structural responses were in close agreement. In particular, not only the load vs displacement curves were highly comparable (general shape, peak loads and displacements at failure correctly predicted), but also the failure mode associated with bending failure was consistently reproduced: indentation under the anvils, damage slowly growing at extrados due to compressive stress, damage due tension quickly propagating at the intrados under the loaded zone in the post-peak regime (data not shown).

3 Results and discussion

3.1 Experimental results and photogrammetric measurements for end-repaired beams

The results of the tests carried out in the Laboratory are shown in Table 3. The experimental data were compared to the expected mean values for timber of class GL28h, estimated by considering the product of the characteristic values by 1.3, which is normally regarded as representing the mean value of a given timber property. Average experimental loads at collapse, i.e., the maximum loads reached during each test (Table 3), evidenced how these values were slightly lower, although comparable, with the mean value expected on the basis of calculations (62.12 kN). This occurrence also reflected on the average flexural stress at collapse, calculated considering a continuous (i.e., not cut) wood section, according to the usual expressions for 4-points bending tests. The experimental average values were included in the range 34.7-36.1 MPa, slightly lower than the expected mean value for timber (36.4 MPa). In fact, only those specimens characterised by the presence of timber-related defects (knots, localised grain deviation, rupture in finger joints etc., observed in series 45/45 and 90/90, Table 3) broke close to the central part of beams, i.e., in the nominally pure bending area.

Moreover, considering that our experimental test arrangement was configured so as to make appreciable the shear stress close to the repaired end-parts (**Fig 1**), it is worth evidencing that the average values of shear stress at collapse, also calculated considering a continuous wood section, that is using the expression $\tau_R = 1.5 \cdot \frac{F_{\max}}{2 \cdot b \cdot h}$, were included in the range 2.3-2.4 MPa, that is below the characteristic value for the considered class (3.5 MPa).

In general, it is possible to state that, although the expected values for the integer beams could not be fully recovered using the adopted technique, they were very close to them.

Concerning the comparison among the considered intervention typologies, some statistical evaluations were carried out using Student-t test (α=0.05) to take account of the usual variability affecting tests on timber. This test showed that the differences in average values of both loads at collapse and stiffness (proportional to the slope of load-deflection curves assessed at mid-span, Table 3) were not statistically significant ($p>>0.05$). This finding clearly indicated that the presence of short screws did not improve the mechanical performance of repaired elements, but they left unaltered both the load at collapse and the stiffness of reinforced beams. Looking at the failure mode, it was observed that beams of series 45/refer collapsed due to the occurrence of splitting invariably localised under the upper rods of the main (longer) part of the beam,

Table 3 - Experimental results obtained for end-repaired beams. UUBB = under the upper bar of the main (longer) part of the beam; ALBB = above the lower bar of the main part of the beam; POLB = pull-out of the lower bars; T = timber-related defects (knots, localised grain deviation, rupture in finger joints etc.). In bold the mechanism observed in the pre-peak regime.

Configuration	Sample	Pmax [kN]	Deflection @ Pmax [mm]	Slope of the load-deflection curve @ mid span, N/mm	Failure modes
45 / refer	T6	65.64	19.7	4244	**UUBB**; POLB
	T9	59.01	18.1	3802	**UUBB**; POLB
	T10	65.08	19.7	3874	**UUBB**; POLB
	T12	57.00	19.8	3583	**UUBB**; POLB
Average		**61.68**	**19.3**	**3876**	
45 / 45	T1	*51.26*	14.7	4004	**T**
	T5	63.36	17.7	4129	**ALBB**; POLB
	T8	*49.87*	15.4	3557	**T**
	T11	65.30	18.1	4302	**ALBB**; POLB
	T13	66.67	N.A.	3730	**ALBB**; POLB
Average		**59.29**	**16.5**	**3945**	
90 / 90	T2	*55.94*	23.1	3452	**T**
	T15	62.35	28.5	3385	**ALBB**
	T16	56.23	17.5	4191	**ALBB**
	T17	64.46	21.4	4241	**ALBB**
	T18	58.89	18.2	4086	**ALBB**
Average		**59.57**	**21.7**	**3871**	

similar to Pizzo et al. [17]. This mechanism was also associated to the pull-out of lower bars, which occurred at the moment of collapse. Instead, in both 45/45 and 90/90 series cracks due to wood splitting moved down towards lower bars, localised at the tips of screws (mechanism ALBB in Table 3). Thus, the presence of screws (although short) affected the failure mechanism of repaired beams.

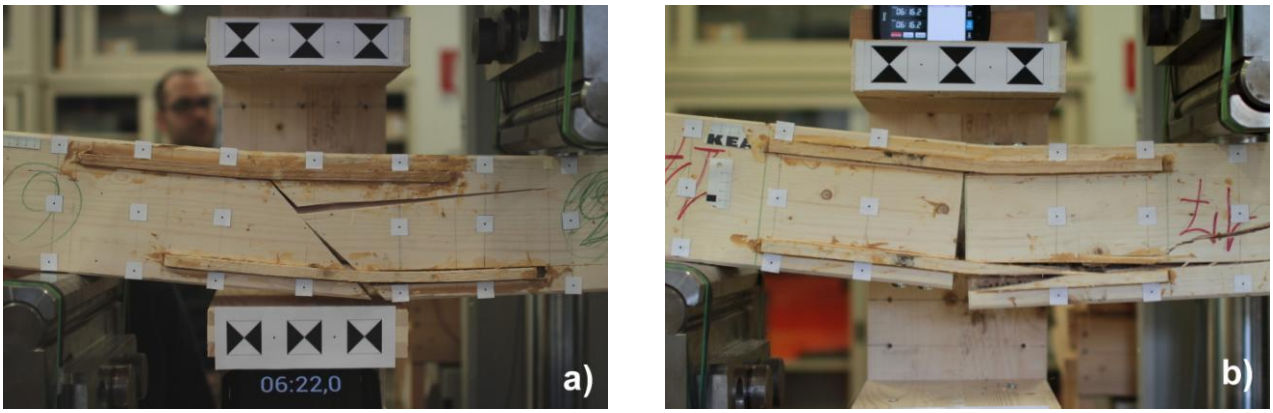

Fig 7 – Examples of failure modes for representative elements: a) UUBB; b) ALBB.

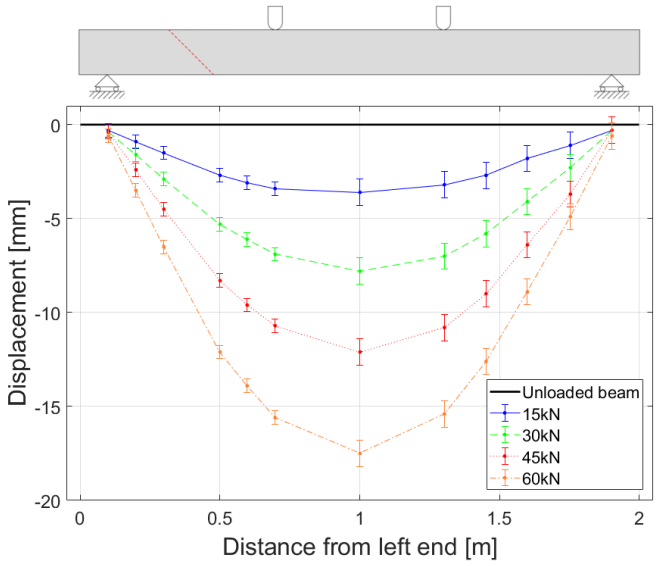

Fig 8 - Photogrammetrically detected deflections of one representative beam of series 45/refer (error bars have been magnified by a factor of two). The left end measurements are more precise due to the smaller pixel size on Canon EOS 7D pictures.

Through the photogrammetric workflow shown in Section 2.2, the displacement of every single marker dot on the beam could be accurately assessed. In particular, the displacement of the intrados points was detected to reconstruct the deformation profile of the beam (**Fig 8**) at a certain applied load step in order to allow some comparisons with the corresponding values computed by the numerical model. The load step increment adopted for this purpose is 15kN.

3.2 Numerical results for the end-repaired beams

The three experimental typologies shown in **Fig 1** have been simulated, and the main mechanical parameters obtained after numerical analysis shown in Table 4. The steel rods and the adhesive have been modelled as elastic-plastic isotropic materials with the material parameters provided by the manufacturers. In particular,

Table 4 - Peak loads, displacements at peaks and failure modes for each numerically simulated configuration.

Configuration	Peak Load [kN]	Displacement [mm]	Failure Mode
45/refer	62.02	17.10	Pull-out of the lower bar in the main beam combined with horizontal crack above the lower bars in the main part of the beam
45/45	61.72	16.46	Pull-out of the lower bar in the main beam combined with horizontal crack above the lower bars in the main part of the beam
90/refer	52.78	15.03	Yielding of the lower bars
90/90	56.43	18.14	Horizontal crack above the lower bars in the main beam
90/90 passing screws S275	60.02	20.38	Yielding of the lower bars
90/90 passing screws B450C	66.64	22.79	Pull-out of the lower bar in the main beam combined with horizontal crack above the lower bars in the main beam
45/refer $f_{t,R} = 0.50$ MPa $f_v = 6.9$ MPa	57.16	17.70	Shear cracks across the cut and horizontal crack above the lower bars in the main beam
45/refer $f_{t,R} = 1.25$ MPa $f_v = 6.9$ MPa	62.86	18.19	Pull-out at the end of the lower bar in the main beam
45/refer $f_{t,R} = 2.50$MPa $f_v = 6.9$ MPa	63.87	17.77	Pull-out at the end of the lower bar in the main beam

the steel and adhesive Young's moduli are 210000 and 4000 MPa, respectively, while the Poisson coefficients are 0.3 and 0.35, respectively. Moreover, steel S275 has been used in all the simulations, except in the case of passing screws as illustrated in Section 3.2.2, where both steel S275 and B450C have been used. For the sake of simplicity, a perfect adhesion has been assumed at the steel-adhesive and the adhesive-wood interfaces. A thin layer made of a linear elastic isotropic material with reduced Young's modulus has been introduced to simulate the unilateral contact at the cut-interface.

As for wood, the parallel-to-grain compressive strength, $f_{c,L}$, and the tensile strength, $f_{t,L}$, have been set to 35 and 65 MPa, respectively, whereas the other parameters are shown in Table 2. More comments on the model sensitivity to the material parameters are given in Section 3.2.4.

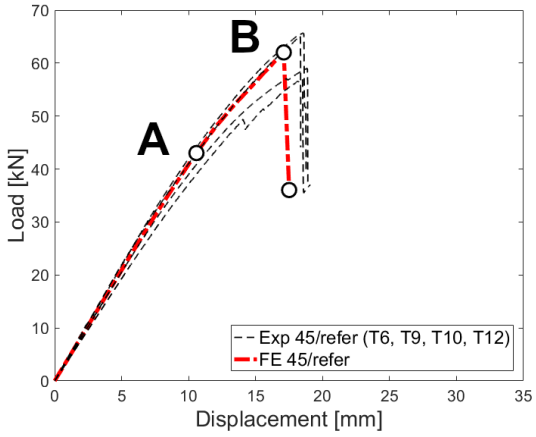

Fig 9 - Comparison between experimental (black dashed line) and numerical (red point-dashed line) load vs deflection curves obtained for 45/refer beam and obtained with $f_{t,L} = 35$ MPa, $f_{c,L} = 65$ MPa, $f_{t,R} = 1.25$ MPa, $f_v = 4$ MPa.

A three-dimensional mesh with 228599 tetrahedrons and a characteristic mesh size of 2 mm has been used. The numerical test took 13 hours. Owing to the symmetry with respect to the LR plane, only one half of the specimen has been modelled.

The experimental and the numerical load vs displacement curves for the 45/refer configuration of **Fig 1a** are displayed in **Fig 9**. It can be drawn that the response of the repaired beam is brittle.

436 **Fig 10** displays the contour plots of the cumulative damage greater than 10^{-3} evaluated at the development of
437 the first macro-crack (Step A), at the peak load (Step B) and at complete failure (Step C).
438

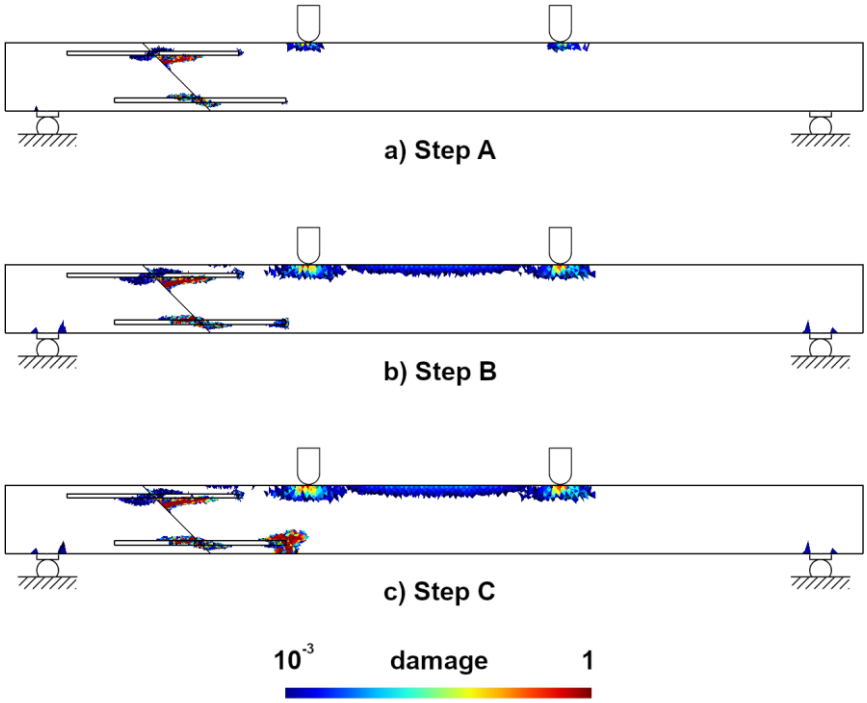

439
440 **Fig 10** - Contour plots of the cumulative damage for the 45/refer beam (**Fig 1a**) at different steps of the load
441 vs displacement curve (**Fig 9**).

442
443 Before the load peak, the contour map of the cumulative damage at Step A displays two horizontal cracks
444 located below the upper bar in the main part of the beam and above the bottom bar in the prosthesis.
445 Furthermore, an indentation process develops under the loaded area. Then, at step B corresponding to the
446 peak reached at load 62.02 kN, the compression generated by the bending starts damaging the upper side of
447 the beam section, while the aforementioned horizontal cracks further propagate. In addition, a damaged zone
448 close to the left end of the lower bar is activated. This latter damage zone spreads at failure, reached at step
449 C, possibly, as a consequence of the pull out of the bars.
450 **Fig 9** and **Fig 10** display a good agreement between the numerical and the experimental results. Both the
451 failure mode and the structural response obtained from the numerical simulation are consistent with those
452 observed in the experimental tests. Particularly interesting is the agreement with the cumulative damage at

453 Step A, where the cracks developing before the maximum load is attained (evidenced both in present and
454 previously reported tests, [17]) are correctly predicted.
455
456 3.2.1 Comparison between numerical results and photogrammetric measurements
457 The displacements of selected points close to the intrados were detected to reconstruct the deformation
458 profile of the 45/refer beam at a predefined load step of 15 kN (Table 5). These displacements are then
459 compared with the values computed by the numerical model. The experimental and the numerical
460 displacement data are in good agreement.
461
462 Table 5 - Comparison between the numerical and the experimental displacement profile for different values
463 of the applied loads for the 45/refer series.

	P=15kN		**P=30kN**		**P=45kN**		**P=59 kN**	
x [mm]	*PHOT [mm]*	*FEM [mm]*	*PHOT [mm]*	*FEM [mm]*	*PHOT [mm]*	*FEM [mm]*	*PHOT [mm]*	*FEM [mm]*
100	0.30 ± 0.18	0.1422	0.40 ± 0.18	0.2872	0.40 ± 0.18	0.5161	0.60 ± 0.18	0.9764
199	0.90 ± 0.18	0.7262	1.60 ± 0.18	1.4668	2.40 ± 0.18	2.5740	3.50 ± 0.18	4.7429
299	1.50 ± 0.18	1.3408	2.90 ± 0.18	2.7084	4.50 ± 0.18	4.7860	6.00 ± 0.18	8.8832
500	2.70 ± 0.18	2.6529	5.30 ± 0.18	5.3595	8.30 ± 0.18	9.5353	12.10 ± 0.18	17.9188
597	3.10 ± 0.18	3.0720	6.10 ± 0.18	6.2056	9.60 ± 0.18	11.3841	13.90 ± 0.18	21.7272
697	3.40 ± 0.35	3.4578	6.90 ± 0.35	6.9847	10.70 ± 0.35	12.8380	15.60 ± 0.35	24.6683
1001	3.60 ± 0.35	3.9006	7.80 ± 0.35	7.8787	12.10 ± 0.35	13.2207	17.50 ± 0.35	23.5521
1303	3.20 ± 0.35	3.4173	7.00 ± 0.35	6.9023	10.80 ± 0.35	11.2025	15.40 ± 0.35	19.2159
1452	2.70 ± 0.35	2.7500	5.80 ± 0.35	5.5543	9.00 ± 0.35	8.9089	12.60 ± 0.35	15.0855
1600	1.80 ± 0.35	1.9824	4.10 ± 0.35	4.0041	6.40 ± 0.35	6.3709	8.90 ± 0.35	10.6981
1754	1.10 ± 0.35	1.0235	2.30 ± 0.35	2.0673	3.70 ± 0.35	3.2646	4.19 ± 0.35	5.4380

464
465
466 3.2.2 Influence of the screws
467 The simulation of the two numerical models related to configurations 45/45 and 90/90 (respectively **Fig 1b**
468 and **Fig 1c**) was made by 315484 and by 297092 tetrahedrons, respectively. It has taken almost 19 hours for
469 the 45/45 configuration and 17 hours for the 90/90 one on a PC i7-5930k CPU.
470 The numerical and the experimental load vs deflection curves are reported in **Fig 11**. For the sake of
471 completeness, the results obtained for the configuration without reinforcing screws have also been reported.

It can be deduced that the screws do not significantly affect the peak load and the brittleness of the structural response of the 45/refer end-repaired beams, whereas they increase the peak load by only 6% in the 90/90 configuration.

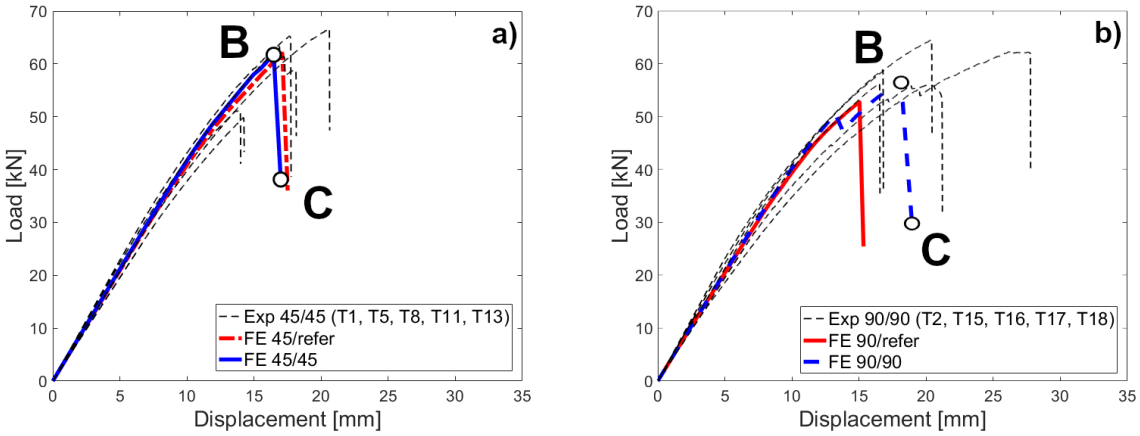

Fig 11 - Comparison between experimental (black dashed line) and numerical load vs displacement curves for: a) the 45/refer (red point-dashed line) and the 45/45 (blu continuous line); b) the 90/refer (red continuos line) and the 90/90 (blu dashed line) configurations. $f_{t,L} = 35$ MPa, $f_{c,L} = 65$ MPa, $f_{t,R} = 1.25$ MPa, $f_v = 4$ MPa.

Fig 12 and **Fig 13** show the contour plots of the cumulative damage for the 45/45 and 90/90 configurations, respectively. In particular, the displayed contour plots correspond to the stages immediately before (a) and at failure (b), namely at steps B and C (**Fig 11**) according to the notation adopted for the 45/refer configuration. Furthermore, a detail of the cumulative damage at failure in the screws section is reported in **Fig 12c** and **Fig 13c**. These contour plots show that, in both the considered configurations, the reinforcing screws stop the crack propagation below the upper rods of the main part of the beam, whereas some damage develops at the screws tips. Moreover, failure occurs around steel bars, as a consequence of either yielding or pull-out-related tensions.

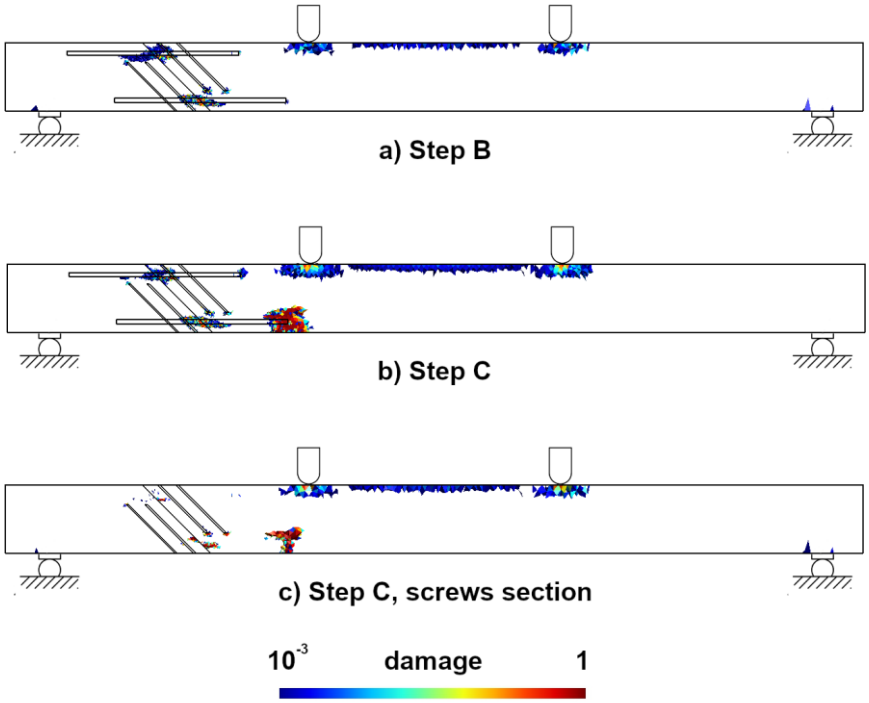

491

492 **Fig 12** – Contour plots of the cumulative damage immediately before (a) and at failure (b) for the 45/45

493 configuration (**Fig 1b**). In (c), the cumulative damage at failure in the screws section is shown.

494

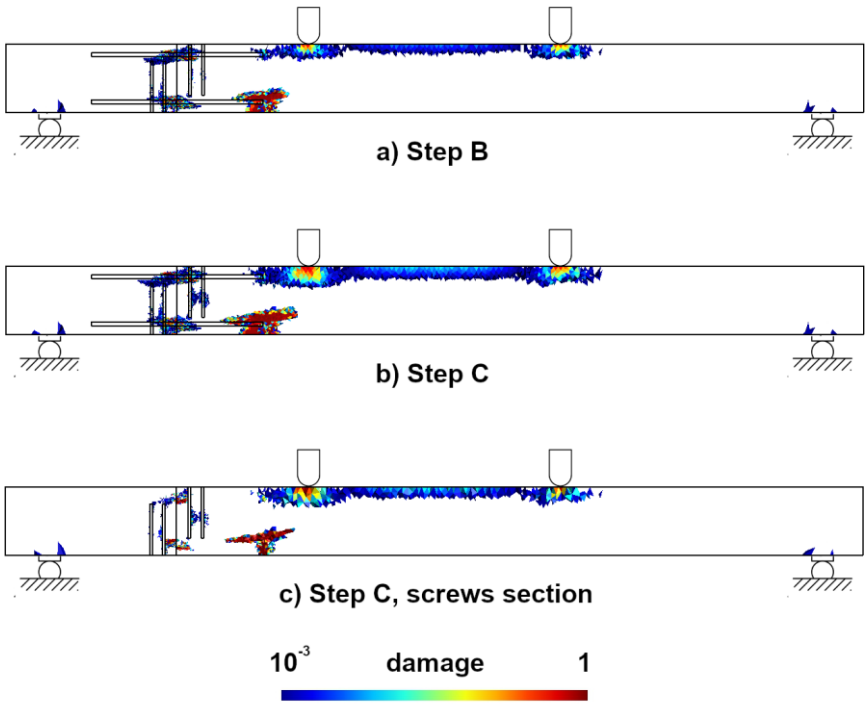

495

496 **Fig 13** - Contour plots of the cumulative damage immediately before (a) and at failure (b) for the 90/90

497 configuration of **Fig 1c**. In (c), the cumulative damage at failure in the screws section is shown.

The results of numerical simulations confirm the experimental evidence that the presence of short reinforcing screws on the load vs displacement curves is marginal for both the 45/45 and 90/90 series. The numerical damage map is also in agreement with the experimentally observed cracking pattern, displaying the movement of the damage zone at failure from the upper bars of the main part of the beams towards the lower ones.

3.2.3 Numerical assessment of the effect of passing screws

Numerical investigation was also used to assess to which extent the usage of passing screws (**Fig 14**) might further improve the structural performance of the end-repaired beams. For this purpose, simulations have been carried out for the case of the 90° cut. In detail, two simulations have been run, one with a steel with yielding stress equal to 275 MPa, the same as used on the experimental tests, and another one with a steel yielding at 450 MPa, the same used in [20], with the aim of assessing the influence of the steel strength on the increase of the peak load. The failure modes detected in the simulations are presented in Table 4.

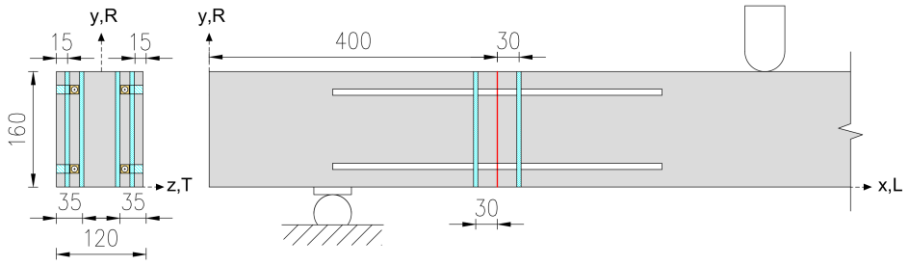

Fig 14 – The configuration with 90° cut and passing screws simulated in the numerical investigation.

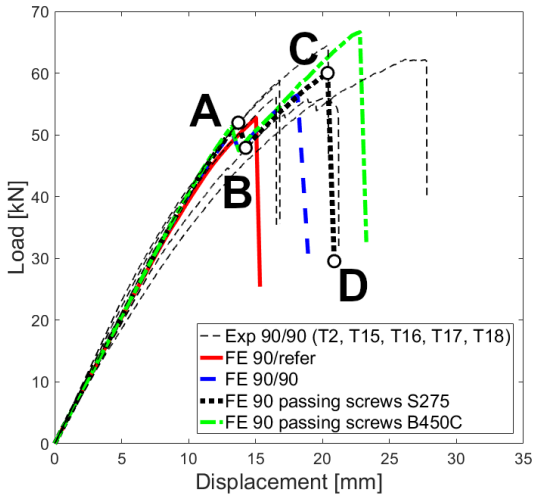

516

517 **Fig 15** – Comparison between numerical load vs displacement curves for the 90° cut beam with passing

518 screws in both cases of steel S275 and B450C, the 90/90 configuration with non-passing screws

519 (experimental tests), and the 90/refer beam. $f_{t,L} = 35$ MPa, $f_{c,L} = 65$ MPa, $f_{t,R} = 1.25$ MPa, $f_v = 4$ MPa.

520

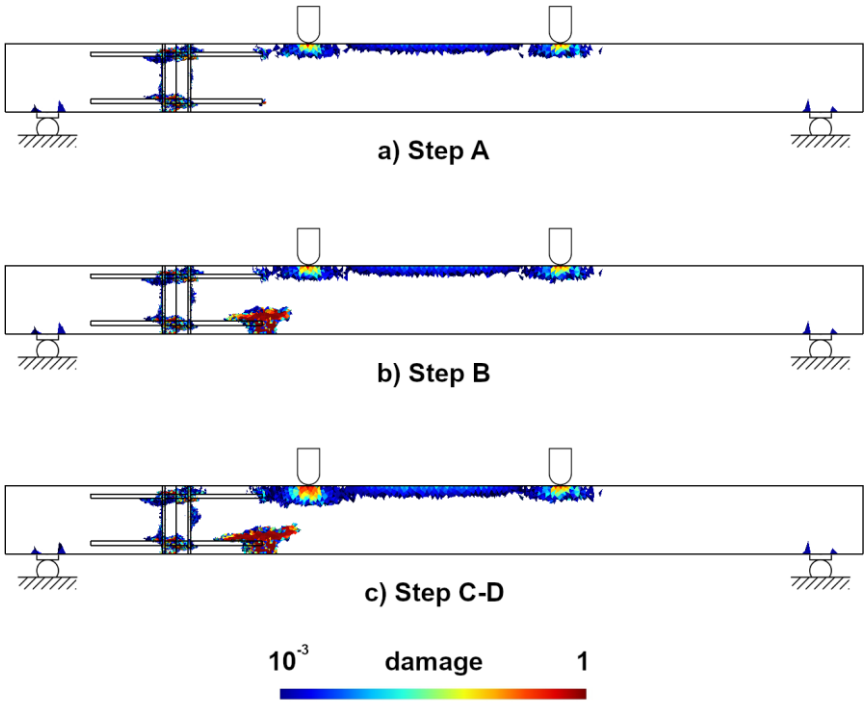

521

522 **Fig 16** - Contour plots of the cumulative damage for the 90° cut beam with passing screws and steel S275.

523

524 **Fig 15** shows that, with respect to the 90/refer beam, the passing screws increase the failure load by 14% in

525 the case of steel S275, namely from 52.78 kN to 60.02 kN, and by 26% in the case of steel B450c, that is

526 from 52.78 kN to 66.64 kN. The damage maps illustrated in **Fig 16** display that, analogously to the non-
527 passing screws, the presence of the passing screws inhibits damage in their surrounding zone: failure starts at
528 step C, completes at step D and occurs by yielding and/or pull-out of the steel bars. On the other hand, it is
529 worth noting that, when screws made of B450C are simulated, the damaged zone developing above the lower
530 bar in the main part of the beam is larger, and failure mainly occurs by pull-out of the lower bar, while the
531 yielding of the latter is still present but to a lesser extent.
532
533 3.2.4 Numerical sensitivity analysis to the orthogonal-to-the-grain tensile strength
534 A sensitivity analysis has been carried out on the 45/refer configuration to assess the influence of the
535 strength properties along the direction orthogonal to the grain, having fixed all the remaining material
536 parameters. In particular, the cases where $f_{t,R} = 0.50, 1.25, 2.50$ MPa with $f_v = 6.9$ MPa have been
537 considered. **Fig 17** compares the experimental and the structural paths computed with the aforementioned
538 parameters. It can be drawn that changing the strength in the radial direction does not significantly alter the
539 load-displacement curves. The corresponding damage maps at failure are displayed in **Fig 18**, and they
540 evidence that the respective damage patterns are markedly different, especially in the case of $f_{t,R} = 0.50$
541 MPa, for which the model predicts diffused shear cracks across the cut that, however, have not been
542 experimentally observed. This circumstance implies that the characteristic value of 0.5 MPa recommended in
543 codes for class GL28h (the same used in present tests) is highly precautionary and not suitable for numerical
544 codes. The failure modes computed for the whole set of constitutive parameters are collected in Table 4. A
545 satisfying correspondence between the numerical and the experimental failure modes can be evidenced.
546
547
548 **4 Conclusions**
549 Some experimental tests were aimed at evaluating the effectiveness of short screws inserted in beams
550 repaired at one end with the use of GIR, to locally reinforce timber in the perpendicular-to-grain direction.
551 Moreover, a comprehensive numerical analysis, supported by photogrammetric measurements, was carried
552 out in order to interpret the experimental behaviour of both reinforced and unreinforced beams.
553

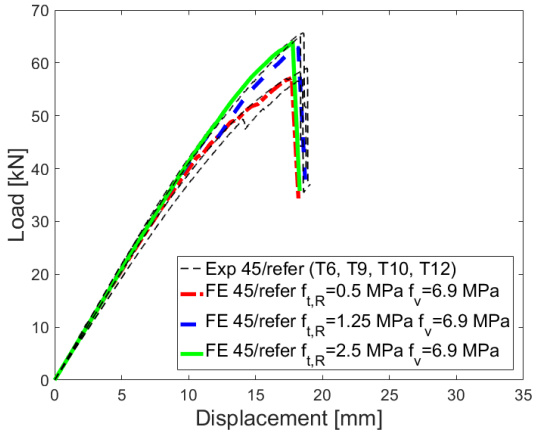

554

555 **Fig 17** - Sensitivity analysis: Influence of the radial tensile strength. $f_{t,R}$ obtained with $f_{t,L} = 35$ MPa,

556 $f_{c,L} = 65$ MPa.

557

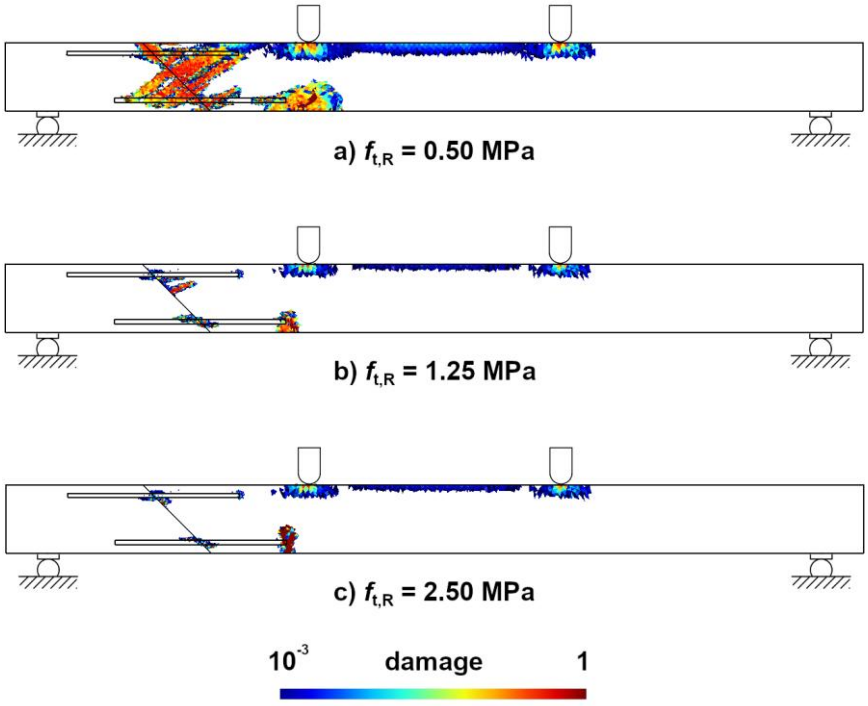

558

559 **Fig 18** - Contour plots of the cumulative damage at failure for the 45/refer beam for variable $f_{t,r}$.

560

561 Results showed that short screws were not able to substantially improve the load capacity of repaired
562 elements, for both configurations 45/45 and 90/90. However, the presence of screws (although short)
563 affected the failure mechanism of repaired beams: the movement of the due-to-splitting cracks towards the

lower bars (of the main part of the beam) was observed in the two screw-reinforced configurations, differently from the 45/refer series where splitting was localised below the upper bars.

Numerical simulation agreed to a very good extent with experimental results (for both screw-reinforced and unreinforced configurations): both the load-displacement curves and the obtained damage maps observed in mechanical tests were correctly predicted, and the deflection behaviour was consistent with the one registered in the photogrammetric survey. Moreover, even when applied to the case, already reported in the literature, of screws passing from extrados to intrados, the numerical model predicted a load capacity increase very close to the one previously reported. Finally, sensitivity analysis allowed establishing that the experimentally observed failure mechanism is related to the failure criteria III/IV, which in fact provides a combination of tension perpendicular-to-grain, longitudinal shear and rolling shear stresses.

Acknowledgements

The Authors are grateful to Piacenti S.r.L. Company (Prato, Italy) for providing the beam samples. Authors express thanks to Paolo Burato, Michele Brunetti and to personnel of the Laboratory of Physical and Mechanical Tests at CNR-IVALSA for their helpful assistance during tests.

References

[1] G. Tampone, N. Ruggieri, State-of-the-art technology on conservation of ancient roofs with timber structure, J. Cult. Herit. 22 (2016) 1019–1027. doi:10.1016/j.culher.2016.05.011.

[2] C. Alessandri, V. Mallardo, Structural assessments of the Church of the Nativity in Bethlehem, J. Cult. Herit. 13 (2012) e61–e69. doi:10.1016/j.culher.2012.10.010.

[3] K.-U. Schober, A.M. Harte, R. Kliger, R. Jockwer, Q. Xu, J.-F. Chen, FRP reinforcement of timber structures, Constr. Build. Mater. 97 (2015) 106–118. doi:10.1016/j.conbuildmat.2015.06.020.

[4] S. Franke, B. Franke, A.M. Harte, Failure modes and reinforcement techniques for timber beams – State of the art, Constr. Build. Mater. 97 (2015) 2–13. doi:10.1016/j.conbuildmat.2015.06.021.

[5] A. Borri, M. Corradi, A. Grazini, A method for flexural reinforcement of old wood beams with CFRP materials, Compos. Part B Eng. 36 (2005) 143–153. doi:10.1016/j.compositesb.2004.04.013.

[6] R. Steiger, E. Serrano, M. Stepinac, V. Rajcic, C. O'Neill, D. McPolin, R. Widmann, Reinforcement with glued-in rods, in: A.M. Harte, P. Dietsch (Eds.), Reinf. Timber Struct. State---Art Rep., Shaker Verlag GmbH, Aachen, Germany, 2015: pp. 133–159.

[7] R. Bainbridge, C. Mettem, K. Harvey, M. Ansell, Bonded-in rod connections for timber structures. Development of design methods and test observations, Int. J. Adhes. Adhes. 22 (2002) 47–59. doi:10.1016/S0143-7496(01)00036-7.

[8] M.A. Parisi, M. Piazza, Restoration and Strengthening of Timber Structures: Principles, Criteria, and Examples, Pract. Period. Struct. Des. Constr. 12 (2007) 177–185. doi:10.1061/(ASCE)1084-0680(2007)12:4(177).
[9] C. Alessandri, V. Mallardo, B. Pizzo, E. Ruocco, The roof of the Church of the Nativity in Bethlehem: Structural problems and intervention techniques, J. Cult. Herit. 13 (2012). doi:10.1016/j.culher.2012.10.013.
[10] M. Del Senno, M. Piazza, R. Tomasi, Axial glued-in steel timber joints. Experimental and numerical analysis, Holz Als Roh- Werkst. 62 (2004) 137–146. doi:10.1007/s00107-003-0450-1.
[11] R. Steiger, E. Gehri, R. Widmann, Pull-out strength of axially loaded steel rods bonded in glulam parallel to the grain, Mater. Struct. 40 (2007) 69–78. doi:10.1617/s11527-006-9111-2.
[12] G. Tlustochowicz, E. Serrano, R. Steiger, State-of-the-art review on timber connections with glued-in steel rods, Mater. Struct. 44 (2011) 997–1020. doi:10.1617/s11527-010-9682-9.
[13] J. Eberhardsteiner, Mechanisches Verhalten von Fichtenholz. Experimentelle Bestimmung der biaxialen Festigkeitseigenschaften, Springer Vienna, Vienna, 2002. http://nbn-resolving.de/urn:nbn:de:1111-20110921173.
[14] T. Vallée, T. Tannert, S. Fecht, Adhesively bonded connections in the context of timber engineering – A Review, J. Adhes. 93 (2017) 257–287. doi:10.1080/00218464.2015.1071255.
[15] M. Stepinac, F. Hunger, R. Tomasi, E. Serrano, V. Rajcic, J.-W. van de Kuilen, Comparison of design rules for glued-in rods and design rule proposal for implementation in European standards, in: R. Görlacher (Ed.), Proc. Int. Counc. Res. Innov. Build. Constr. Work. Comm. W18 - Timber Struct. CIB-W18 Meet. 46 26-29 August 2013 Vanc., Timber Scientific Publishing, Karlsruhe, Germany, 2013: p. CIB-W18/46-7-10.
[16] EN 1995-2, Eurocode 5: Design of timber structures - Part 2: Bridges, European Committee for Standardization CEN, Brussels, 2004.
[17] B. Pizzo, M. Gavioli, M.P. Lauriola, Evaluation of a design approach to the on-site structural repair of decayed old timber end beams, Eng. Struct. 48 (2013) 611–622. doi:10.1016/j.engstruct.2012.09.036.
[18] C. O'Neill, D. McPolin, S.E. Taylor, T. Martin, A.M. Harte, Glued-in basalt FRP rods under combined axial force and bending moment: An experimental study, Compos. Struct. 186 (2018) 267–273. doi:10.1016/j.compstruct.2017.12.029.
[19] N. Gattesco, A. Gubana, M. Buttazzi, M. Melotto, Experimental investigation on the behavior of glued-in rod joints in timber beams subjected to monotonic and cyclic loading, Eng. Struct. 147 (2017) 372–384. doi:10.1016/j.engstruct.2017.03.078.
[20] A. Susini, Ripristino strutturale di travi lignee: indagine sugli interventi di ricostruzione di testata con protesi di legno connessa con barre incollate, M.Sc. Thesis, Firenze, 2013.
[21] S.W. Tsai, E.M. Wu, A General Theory of Strength for Anisotropic Materials, J. Compos. Mater. 5 (1971) 58–80. doi:10.1177/002199837100500106.
[22] R. Hill, A Theory of the Yielding and Plastic Flow of Anisotropic Metals, Proc. R. Soc. Math. Phys. Eng. Sci. 193 (1948) 281–297. doi:10.1098/rspa.1948.0045.
[23] A. Bouchaïr, A. Vergne, An application of the Tsai criterion as a plastic flow law for timber bolted joint modelling, Wood Sci. Technol. 30 (1995) 3–19. doi:10.1007/BF00195264.
[24] P.L. Clouston, F. Lam, A stochastic plasticity approach to strength modeling of strand-based wood composites, Compos. Sci. Technol. 62 (2002) 1381–1395. doi:10.1016/S0266-3538(02)00086-6.
[25] R. De Borst, P.H. Feenstra, Studies in anisotropic plasticity with reference to the Hill criterion, Int. J. Numer. Methods Eng. 29 (1990) 315–336. doi:10.1002/nme.1620290208.
[26] O. Hoffman, The Brittle Strength of Orthotropic Materials, J. Compos. Mater. 1 (1967) 200–206. doi:10.1177/002199836700100210.
[27] B.H. Xu, M. Taazount, A. Bouchaïr, P. Racher, Numerical 3D finite element modelling and experimental tests for dowel-type timber joints, Constr. Build. Mater. 23 (2009) 3043–3052. doi:10.1016/j.conbuildmat.2009.04.006.
[28] P. Mackenzie-Helnwein, J. Eberhardsteiner, H.A. Mang, A multi-surface plasticity model for clear wood and its application to the finite element analysis of structural details, Comput. Mech. 31 (2003) 204–218. doi:10.1007/s00466-003-0423-6.
[29] J. Schmidt, M. Kaliske, Zur dreidimensionalen Materialmodellierung von Fichtenholz mittels eines Mehrflächen-Plastizitätsmodells, Holz Als Roh- Werkst. 64 (2006) 393–402. doi:10.1007/s00107-006-0102-3.

[30] C. Sandhaas, J.W.G. van de Kuilen, H.J. Blass, Constitutive model for wood based on Continuum Damage Mechanics, in: P. Quenneville (Ed.), Proc. World Conf. Timber Eng. 2012 WCTE 2012 Auckl. N. Z. 15-19 July 2012, Curran, Red Hook, NY, 2012: pp. 159–167.
[31] C. Sandhaas, J.W.G. van de Kuilen, Material model for wood, Heron. 58 (2013) 171–192.
[32] Z.P. Bažant, B.H. Oh, Crack band theory for fracture of concrete, Matér. Constr. 16 (1983) 155–177. doi:10.1007/BF02486267.
[33] E. Benvenuti, B. Loret, A. Tralli, A unified multifield formulation in nonlocal damage, Eur. J. Mech. - ASolids. 23 (2004) 539–559. doi:10.1016/j.euromechsol.2004.03.005.
[34] E. Benvenuti, G. Borino, A. Tralli, A thermodynamically consistent nonlocal formulation for damaging materials, Eur. J. Mech. - ASolids. 21 (2002) 535–553. doi:10.1016/S0997-7538(02)01220-2.
[35] L.F. Sirumbal-Zapata, C. Málaga-Chuquitaype, A.Y. Elghazouli, A three-dimensional plasticity-damage constitutive model for timber under cyclic loads, Comput. Struct. 195 (2018) 47–63. doi:10.1016/j.compstruc.2017.09.010.
[36] A. Khennane, M. Khelifa, L. Bleron, J. Viguier, Numerical modelling of ductile damage evolution in tensile and bending tests of timber structures, Mech. Mater. 68 (2014) 228–236. doi:10.1016/j.mechmat.2013.09.004.
[37] B. Pizzo, K.-U. Schober, On site interventions on decayed beam-ends, in: M. Dunky, B. Källander, M. Properzi, K. Richter, M. Van Leemput (Eds.), Core Doc. COST Action E34 Bond. Timber, Univerität für Bodenkultur, Vienna, 2008: pp. 40–49.
[38] B. Pizzo, M.P. Lauriola, Repair of timber end-beams: Some operational aspects, in: F.M. Mazzolani (Ed.), Proc. 1st Int. Conf. "Protection Hist. Build. PROHITECH 09" Rome 21-24 June 2009, CRC Press/Balkema, Taylor & Francis Group, Leiden, The Netherlands, 2009: pp. 397–402.
[39] P. Rönnholm, M. Nuikka, A. Suominen, P. Salo, H. Hannu, P. Pöntinen, H. Haggrén, M. Vermeer, J. Puttonen, H. Hirsi, A. Kukko, H. Kaartinen, J. Hyyppä, A. Jaakkola, Comparison of measurement techniques and static theory applied to concrete beam deformation, Photogramm. Rec. 24 (2009) 351–371. doi:10.1111/j.1477-9730.2009.00548.x.
[40] S.J. Gordon, D.D. Lichti, J. Franke, M.P. Stewart, Measurement of Structural Deformation using Terrestrial Laser Scanners, in: 2004.
[41] S.J. Gordon, D.D. Lichti, M.P. Stewart, J. Franke, Structural Deformation Measurement using Terrestrial Laser Scanners, in: S.C. Stiros, S. Pytharouli (Eds.), 2003: pp. 185–192.
[42] M.R. Kaloop, A.A. Beshr, M.Y. Elshiekh, Using Total Station for monitoring the deformation of high strength concrete beams, in: 2008: pp. 411–419.
[43] I. Detchev, A. Habib, M. El-Badry, Estimation of vertical deflections in concrete beams through digital close range photogrammetry, ISPRS - Int. Arch. Photogramm. Remote Sens. Spat. Inf. Sci. XXXVIII-5/W12 (2012) 219–224. doi:10.5194/isprsarchives-XXXVIII-5-W12-219-2011.
[44] I. Detchev, A. Habib, M. El-Badry, Case study of beam deformation monitoring using conventional close range photogrammetry, in: 2011: p. un-paginated CD Rom.
[45] T. Whiteman, D.D. Lichti, I. Chandler, Measurement of Deflections in Concrete Beams by Close-Range Photogrammetry, in: 2002: p. vol. XXXIV, Part 4.
[46] J. Valença, E.N.B.S. Júlio, H.J. Araújo, Applications of Photogrammetry to Structural Assessment, Exp. Tech. 36 (2012) 71–81. doi:10.1111/j.1747-1567.2011.00731.x.
[47] D.C. Brown, Close-range camera calibration, Photogramm. Eng. 37 (1971) 855–866.
[48] D.E. Kretschmann, Chapter 5. Mechanical properties of wood, in: Forest Products Laboratory (Ed.), Wood Handb. Wood Eng. Mater. Centen. Ed. Gen. Tech. Rep. FPL-GTR-190, U.S. Department of Agriculture, Forest Service, Madison, WI, 2010: pp. 5.1-5.46.